IEEE Access
Multidisciplinary ⋮ Rapid Review ⋮ Open Access Journal

Received February 3, 2020, accepted February 9, 2020, date of publication February 17, 2020, date of current version February 27, 2020.

Digital Object Identifier 10.1109/ACCESS.2020.2974238

Second-Order Sliding Mode-Based Direct Torque Control of Variable-Flux Memory Machine

WEI WANG[1,2], (Student Member, IEEE), HEYUN LIN[1], (Senior Member, IEEE), HUI YANG[1], (Member, IEEE), WEI LIU[1], (Student Member, IEEE), AND SHUKANG LYU[1]

[1]School of Electrical Engineering, Southeast University, Nanjing 210096, China
[2]Department of Information Engineering, Ordos Institute of Technology, Ordos 017000, China

Corresponding author: Heyun Lin (hyling@seu.edu.cn)

This work was supported in part by the National Natural Science Foundation of China under Grant 51377020, and in part by the Research Program of Science and Technology at Universities of Inner Mongolia Autonomous Region under Grant NJZY17409.

ABSTRACT The variable-flux memory machine (VFMM) exhibits high efficiency over a wide speed range because its airgap magnetic flux can easily be regulated by varying the magnetization state (MS) of the employed low coercivity force permanent magnets. This paper proposes a second-order sliding mode (SM)-based direct torque control (DTC) strategy for the VFMM, which features a relatively low computational complexity and less dependence on machine parameters. The operating principle and mathematical model of the VFMM are first described and established. On this basis, a novel control scheme combining the DTC strategy with MS manipulation is proposed, in which the machine is controlled by utilizing the DTC strategy incorporating the $i_d = 0$ condition, while the MS manipulation is implemented by energizing reference stator flux linkage pulses. A super-twisting second-order SM controller is subsequently developed to achieve strong robustness. The developed control structure avoids a complicated decoupling algorithm and is simpler than that of the conventional field-oriented control (FOC) method. Finally, the effectiveness of the proposed control scheme is validated by simulation and experimental results.

INDEX TERMS Direct torque control, magnetization state, strong robustness, super-twisting sliding mode control, variable-flux memory machine.

I. INTRODUCTION

The permanent magnet (PM) synchronous machine (PMSM) has been widely used for various applications due to its inherent merits such as an unsurpassed efficiency and power density [1], [2]. It is becoming increasingly more attractive for traction applications especially for electric vehicles (EVs) [3], [4], in which an extended constant power speed range (CPSR) is significantly desired for cruising operation [5]. To achieve this aim, the conventional flux-weakening (FW) method is traditionally employed by utilizing a negative d-axis current to counteract the PM flux linkage [6]. However, the continuous FW current results in additional energy losses and efficiency reductions. Recently, a variable-flux memory machine (VFMM) employing low coercive force (LCF) PMs has gradually become a competent candidate to realize convenient flux regulation by applying a temporary demagnetizing or magnetizing current pulse [7], [8].

The associate editor coordinating the review of this manuscript and approving it for publication was Ramani Kannan.

VFMMs can be classified into AC and DC types according to their magnetizing current pattern [9]. The PMs of the AC-type VFMMs are normally on the rotor, while those of the DC-type are on the stator. Compared with traditional PM machines, VFMMs can be more flexibly controlled due to their variable PM flux. However, more challenges are also introduced at the same time. Some control methods for VFMMs have been comprehensively investigated in recent years. An on-line magnetization method for a fractional-slot concentrated-winding memory machine was proposed in [11], while an observer-based current decoupling method was proposed in [12] to achieve a smooth torque during the magnetizing manipulation process under loaded conditions. In [13], a hysteresis PI-based algorithm that achieves an improved efficiency and a reduced loss compared to the fixed magnetization state (MS) control was introduced to select the optimal MS during a driving cycle. A straight-line stationary frame flux linkage trajectory ($SL\lambda^sT$) was introduced for higher speed capability and evaluated along with the d-axis pulse and the synchronous frame voltage cancellation

trajectory [14]. A closed-loop MS control method, which adopts the dead-beat direct torque flux control (DB-DTFC) at low speeds and the modified $SL\lambda^{s}T$ at high speeds, was presented in [15]. In addition, the driving cycle loss reduction capability and the thermal impact were also evaluated based on the nonlinear model by using a structured neural network (SNN). The magnet temperature effects on the maximum torque property and magnetizing manipulation were evaluated, and a closed-loop method for mitigation was proposed in [16]. It was shown that the vector control was effective for the characterization of a variable flux machine [17]. A modified adaptive nonlinear filter (MANF) was utilized to instantaneously estimate the flux linkage from the major induced electromotive force (EMF) harmonic components instead of the conventional fundamental component in [18]. A control scheme employing an artificial neural network (ANN) with the maximum torque per ampere (MTPA) was proposed for loss reduction in [19], in which the MS switch signals were generated by calculating the DC-link voltage margin ratio. The ANN exhibited an excellent capability in reducing the inductance nonlinearity effect under different MSs. A control strategy for a doubly salient memory machine (DSMM) was presented in [20]. Furthermore, a dual-mode operation, i.e., doubly salient PM (DSPM) mode or switched reluctance mode, was implemented in [21]. A pole-changing function was realized by employing a set of separate magnetizing windings in [22]. A multimode design methodology of a flux-controllable stator-PM memory motor (FC-SPMMM) under the multiple operation conditions in vehicle driving cycles was proposed in [23]. A stepwise magnetization control strategy and the influences of the design parameters on the demagnetization behavior for a switched flux memory machine (SFMM) were reported in [9-10]. A speed-region-based FW control combined with an MS manipulation method for a hybrid PM axial field flux-switching memory machine was presented, and an adaptive observer was utilized to mitigate the flux linkage estimation error in [24].

Based on the abovementioned research, various control strategies and parameter estimation methods for different VFMMs have been well studied. However, most of them are based on the FOC theory, which has the drawbacks of a relatively sophisticated decoupling algorithm and a high dependence on the machine and controller parameters. Therefore, it is necessary to develop a novel control scheme with a simple structure and less sensitivity to the machine parameters while maintaining a wide CPSR, which is the main purpose of this paper.

Some studies have shown that excellent dynamic performance can be achieved by utilizing a torque and flux regulator without rotor flux orientation and a high dependence on the machine parameters [25], [26]. A direct torque control (DTC) with MTPA strategy for a PMSM under an M-T frame requiring only three parameters of the controlled machine was investigated in [27], [28]. In [29], [30], the DTC-based FW control performance of a PMSM was examined, and the proposed control method was proven to be insensitive to parameter variation, simple and stable. However, some disturbances still exist in the DTC system, e.g., the temperature dependence of the stator resistance and the observation error. To obtain the torque performance with a strong robustness, the variable structure (VS) or sliding mode control (SMC) strategy is a preferred scheme. A nonlinear sliding mode control method was proposed for torque and flux ripple minimizations while preserving the fast responses and robustness merits in [31]. An SMC incorporating the MTPA trajectory scheme was investigated in [32], and an SMC observer for accurate flux estimation at very low speeds was presented in [33]. It is indicated that the SMC is suitable for nonlinear systems due to its outstanding characteristics of simple implementation, strong robustness and rapid response [34].

This paper proposes a second-order sliding mode (SM)-based DTC strategy for VFMM to achieve a wide speed range, high efficiency, and strong robustness performance. The operation principle and mathematical model of a VFMM with hybrid magnetic circuits are first introduced and established. A novel control scheme combining DTC with MS manipulation is proposed to extend the CPSR of the machine. In the proposed scheme, a method of DTC incorporating the $i_{\mathrm{d}} = 0$ condition is utilized under normal operation, and DTC-based flux-weakening or flux-strengthen (FS) temporary pulses are energized in MS manipulations. In addition, a super-twisting SM controller is developed to reduce the influence of system parameter variations. The proposed control scheme avoids continuous magnetizing currents, and the complicated decoupling algorithm with a simplified control structure exhibits independence from the machine's inductance and is less sensitive to load fluctuations.

II. VARIABLE-FLUX MEMORY MACHINE

A. MACHINE TOPOLOGY

The studied VFMM is simultaneously equipped with a high coercive force (HCF) PM NdFeB and an LCF PM AlNiCo. The magnetic properties of the two kinds of PMs are shown in Fig. 1. It can be seen that the hysteresis model of AlNiCo can be approximately characterized by a parallelogram curve, while that of NdFeB can be characterized by a straight line. The MS of AlNiCo can be varied and memorized along the loops of the hysteresis curve and recoil lines by applying a demagnetizing or magnetizing current pulse. The curves of the initial magnetization, major loop and one of the MS manipulation loops are also shown in the figure.

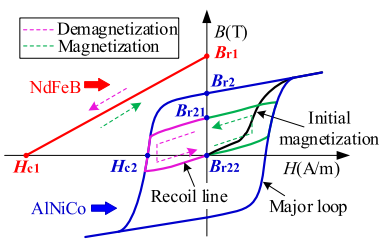

FIGURE 1. Magnetic properties of the NdFeB and AlNiCo PMs.

The cross-section and configuration of the VFMM are illustrated in Fig. 2. The machine features an interior PM (IPM) structure with hybrid PMs, i.e., NdFeB and AlNiCo. The two kinds of PMs are in parallel on the magnetic circuit. The LCF PMs can be either demagnetized or magnetized by applying a negative or positive current pulse to achieve flexible flux regulation. Therefore, the NdFeB PMs act as the constant dominant portion, while the AlNiCo PMs act as the variable adjustment portion of the magnetic flux.

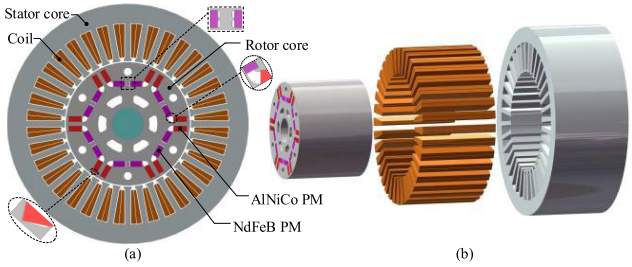

FIGURE 2. The proposed VFMM. (a) Cross section. (b) Configuration.

B. OPERATING PRINCIPLE

The MS of the LCF PMs is an additional control degree-of-freedom for the VFMM compared with the conventional IPM. The MS manipulation principle of the VFMM is shown in Fig. 3. During normal operation periods, the machine adopts a control method of DTC incorporating the $i_d = 0$ condition to avoid unexpected MS changes. A reference flux pulse is applied to engender a transient i_d current pulse. Consequently, the MS of the LCF PMs is reasonably changed to provide a desired speed and torque.

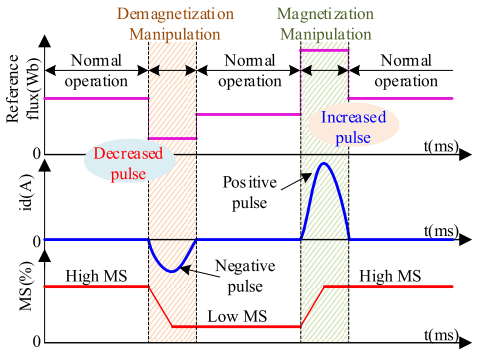

FIGURE 3. The MS manipulation principle of the VFMM.

As illustrated in Fig. 3, the machine starts up with a high MS, and the induced EMF increases with speed. When the terminal voltage of the machine under a high-speed light-load state reaches the DC-link voltage limit, a demagnetizing manipulation (DMM) will be conducted to further increase the speed. A negative i_d pulse induced by the decreased reference flux is utilized to reduce the MS of the LCF magnets. A low MS is achieved when the i_d amplitude reaches the required DMM value, and this state will be held until the next MS. Similarly, a re-magnetizing manipulation (RMM) is employed to gain a high MS suitable for low-speed heavy-load operation.

The magnetization state can be defined as

$$\mathrm{MS} = \frac{B}{B_{\max}} \times 100\% \tag{1}$$

where B and $B_{\max}$ are the present and maximum values of the average air-gap magnetic flux densities under no-load, respectively. The magnetic flux distributions of the machine with 100% and 0% MSs under the no-load situation are shown in Fig. 4.

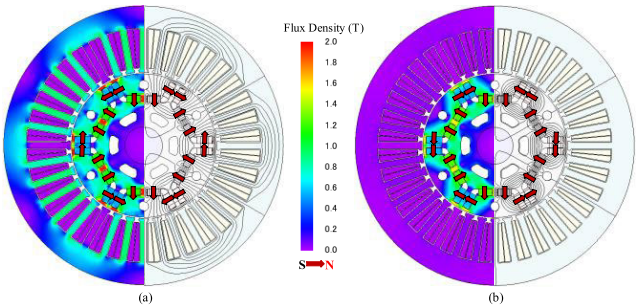

FIGURE 4. The no-load magnetic flux distributions of different MSs. (a) MS = 100%. (b) MS = 0%.

The magnetic flux of the machine can be weakened or strengthened by the addition of constant and variable PM fluxes. When the polarities of the two kinds of PMs are identical, the magnetic flux achieves the maximum value, i.e., 100% MS, as shown in Fig. 4(a). The polarity of the LCF PMs may reverse when an excessive DMM pulse is applied, as shown in Fig. 4(b). Consequently, most magnetic fluxes of the PMs close in the rotor, which is defined as 0% MS. Therefore, the CPSR of the machine can be extended if an appropriate MS is selected.

C. MATHEMATICAL MODEL

This paper proposes a DTC-based MS manipulation scheme which can be implemented in a stator reference frame. Fig. 5 illustrates the flux linkages in the stationary reference frame ($\alpha\beta$), stator reference frame (xy) and rotor reference frame (dq), where $\boldsymbol{\psi}_s$ and $\boldsymbol{\psi}_r$ are the stator and rotor flux linkage vectors, respectively. The angle between them is defined as the load torque angle δ, which equals the summation of θ_{ui} and θ_{ei}. Here, θ_{ui} is the angle between the voltage and current, while θ_{ei} is the angle between the no-load induced EMF and current.

The rotor flux linkage of the VFMM is an additional variable compared with the conventional PMSM. In the stator reference frame, its voltage equations can be expressed as

$$\begin{cases} u_{sx} = R_s i_{sx} + \dfrac{d\psi_s}{dt} \\ u_{sy} = R_s i_{sy} + (\dfrac{d\delta}{dt} + \omega_r)\psi_s \end{cases} \tag{2}$$

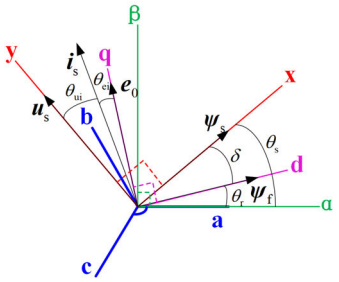

FIGURE 5. The flux linkages in the reference frames.

where u_{sx} and u_{sy} are the x/y-axis voltages, i_{sx} and i_{sy} are the x/y-axis currents, R_s is the stator winding resistance, ψ_s is the amplitude of the stator flux linkage, and ω_r is the rotor angular speed, which is related to stator angular speed ω_s:

$$\omega_s = d\delta/dt + \omega_r \tag{3}$$

The flux linkage equations can be presented as

$$\begin{bmatrix} \psi_{sx} \\ \psi_{sy} \end{bmatrix} = \begin{bmatrix} L_d \cos^2\delta + L_q \sin^2\delta & (L_q - L_d)\sin\delta\cos\delta \\ (L_q - L_d)\sin\delta\cos\delta & L_q \cos^2\delta + L_d \sin^2\delta \end{bmatrix} \times \begin{bmatrix} i_{sx} \\ i_{sy} \end{bmatrix} + \psi_f \begin{bmatrix} \cos\delta \\ -\sin\delta \end{bmatrix} \tag{4}$$

where ψ_f is the PM flux linkage, ψ_{sx} and ψ_{sy} are the x/y-axis flux linkages, and L_d and L_q are the d/q-axis inductances. ψ_f is a function of MS and can be divided into two parts:

$$\psi_f = \psi_{f1} + k\psi_{f2} \tag{5}$$

where ψ_{f1} and ψ_{f2} represent the flux linkage of the NdFeB PM and the AlNiCo PM, respectively; and k is the magnetization ratio (MR), the value range of which is $-1 \le k \le 1$, where $k = 1$ corresponds to 100% MS, and $k = -1$ corresponds to 0% MS.

When the stator flux linkage is aligned with the x-axis, $\psi_{sy} = 0$. Hence, the current equations can be deduced as

$$\begin{cases} i_{sx} = \dfrac{2\psi_f \sin\delta - [(L_d + L_q) + (L_d - L_q)\cos 2\delta] i_{sy}}{(L_d - L_q)\sin 2\delta} \\ i_{sy} = \dfrac{1}{2L_d L_q}[2\psi_f L_q \sin\delta - |\boldsymbol{\psi}_s|(L_q - L_d)\sin 2\delta] \end{cases} \tag{6}$$

The torque T_e can be obtained as

$$T_e = \frac{3}{2} p\psi_s i_{sy} = \frac{3p}{4L_d L_q}\psi_s[2\psi_f L_q \sin\delta - \psi_s(L_q - L_d)\sin 2\delta] \tag{7}$$

where p is the number of pole pairs.

III. PROPOSED CONTROL STRATEGY

A novel control strategy combined DTC with MS manipulation is proposed for the VFMM to extend the CPSR. The block diagram of the overall control scheme is shown in Fig. 6.

The system is composed of a VFMM, an inverter, a detection module, an observer, a command unit, and a torque-flux regulator. An encoder is mounted on the VFMM, and

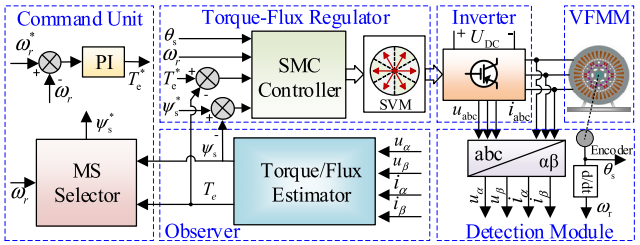

FIGURE 6. Block diagram of the overall control scheme for the VFMM.

the inverter employs the conventional three-phase full-bridge mode. The command unit is in charge of generating the reference torque and flux signals according to the observer and detection module. An MS selector and a proportional integral (PI) controller are utilized to offer the reference flux and torque, respectively. The torque-flux regulator mainly deals with the DTC algorithm, which eliminates the need to consider the varied inductance under different MSs of the VFMM. The method in which the DTC incorporates the $i_d = 0$ condition is utilized during normal operations, and the reference flux-weakening or flux-strengthening pulses are energized under MS manipulation processes. An SMC strategy is developed to mitigate the influence of system parameter fluctuations, e.g., load change. The proposed strategy retains the advantages of DTC, including its rapid response and lower sensitivity to machine parameters. Meanwhile, the air-gap magnetic flux can be flexibly varied by regulating the reference flux pulses to achieve an effective extension of the CPSR with an improved efficiency.

A. DTC WITH $I_d = 0$ METHOD

When the VFMM is fed by a three-phase full-bridge inverter, there are two zero voltage vectors (VVs): $\boldsymbol{u}_0$ (000) and $\boldsymbol{u}_7$ (111); and six non-zero VVs: $\boldsymbol{u}_1$(100), $\boldsymbol{u}_2$(110), $\boldsymbol{u}_3$(010), $\boldsymbol{u}_4$(011), $\boldsymbol{u}_5$(001) and $\boldsymbol{u}_6$(101), as illustrated in Fig. 7. Hence, the stator voltage can be regulated by the status of the power switches, and the stator flux linkage can be obtained by the integral of the stator voltage. It is feasible to form a quasi-circular stator flux linkage trajectory by rapidly and alternately outputting a limited number of VVs. As shown in Fig. 7, the stator flux linkage fluctuates at the radius of ψ_s^* with an error band of $2\Delta\psi_s$. The trajectory will be closer to a circle if more VVs are involved or the vector table is

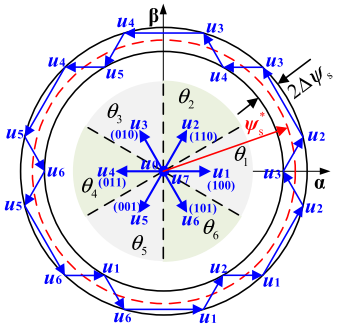

FIGURE 7. Voltage vectors and stator flux linkage trajectory.

optimized by utilizing zero VVs. Therefore, the stator flux linkage can be effectively regulated through space vector modulation (SVM).

To avoid improper MS manipulation of the VFMM, an $i_d = 0$ control condition is added to the abovementioned DTC strategy. An optimal scheme of VVs is selected for the sake of rapidly changing the electromagnetic torque while maintaining $i_d = 0$. The flux linkage and torque in the rotor reference frame can be expressed as

$$\begin{cases} \psi_d = L_d i_d + \psi_f \\ \psi_q = L_q i_q \\ T_e = \dfrac{3}{2} p(\psi_d i_q - \psi_q i_d) \end{cases} \tag{8}$$

where ψ_d and ψ_q are the d/q-axis flux linkages, and i_d and i_q are the d/q-axis currents. The stator flux linkage can be easily obtained as

$$\psi_s = \sqrt{\psi_d^2 + \psi_q^2} \tag{9}$$

Under the condition of $i_d = 0$, ψ_s can be deduced as

$$\psi_s = \sqrt{(2L_q T_e / 3p\psi_f)^2 + \psi_f^2} \tag{10}$$

It can be seen from (10) that T_e is the only variable associated with ψ_s, which can be calculated and estimated within each control cycle of the DTC system. Therefore, ψ_s under the condition of $i_d = 0$ can be achieved according to (10) during each cycle. The proposed method realizes rapid torque control by calculating the corresponding value of ψ_s. By utilizing the torque-flux dual-loop regulation, the advantages of $i_d = 0$ and the rapid dynamic characteristic of DTC can be retained at the same time.

B. MS MANIPULATION

The stator voltage is proportional to the stator flux linkage and the rotor angular speed when the stator resistance is neglected. It can be presented as

$$\begin{aligned} u_s &= \omega_r \psi_s \\ &= \omega_r \sqrt{(\psi_f + L_d i_d)^2 + (L_q i_q)^2} \end{aligned} \tag{11}$$

The stator terminal voltage reaches the maximum value of the inverter voltage U_{smax} when the speed increases to the rated value. The stator flux should be reduced accordingly if the speed range needs to be extended above the rated speed. According to (8) and (9), the flux and torque correspond with the i_d and i_q currents, respectively, so that the d/q-axis currents can be regulated by manipulating the reference flux linkage when the torque remains constant in a short period. For instance, a negative d-axis current can be obtained if the stator flux linkage is reduced in the FW region. The current trajectories during the MS manipulation processes in the d/q plane are illustrated in Fig. 8.

The d-axis current i_d equals 0 during normal operation, which makes the current trajectory move along the q-axis within a current limit. The value of the q-axis current i_q

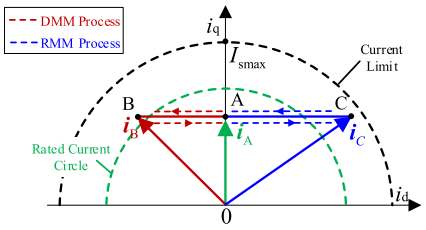

FIGURE 8. Current trajectories during MS manipulation processes.

remains unchanged during a short period of MS manipulation. Consequently, the current vector varies only in the horizontal direction, e.g., the working point moves from A to B and C during the DMM and RMM procedures, respectively. The stator flux linkage can be deduced from (8) and (9) as

$$\psi_s = \sqrt{(L_d i_d + \psi_f)^2 + \left(\frac{2T_e L_q / 3p + L_q(L_q - L_d) i_d}{\psi_f}\right)^2} \tag{12}$$

According to (12), the stator flux linkage ψ_s corresponds to both i_d and ψ_f varying with i_d. It means that there is a one-to-one correspondence between ψ_s and i_d. The PM flux linkage ψ_f can thus be modified by utilizing a reference flux linkage pulse during the MS manipulation processes.

Fig. 9 shows the torque-flux (T_e-ψ_s) trajectories of the VFMM under different MSs, i.e., under different i_ds. The reference torque is set as T_1. Lines AB and CD represent the initial 100% MS and final 0% MS, respectively, during the DMM process, as illustrated in Fig. 9(a). A reduced reference stator flux linkage pulse is applied to realize the DMM while maintaining a constant reference torque in a short period. For instance, the amplitude of the reference stator flux linkage decreases from $|\psi_{s1}|$ to $|\psi_{s2}|$ and is then restored to $|\psi_{s3}|$. This procedure can be accomplished within a period of 100 ms. $|\psi_{s3}|$ is the required stator flux linkage after the DMM, which can be obtained according to (10). The red dashed line (EFG) in Fig. 9(a) represents the trajectory of the DMM process. The normal DTC with $i_d = 0$ method is adopted when a DMM procedure is accomplished. The different ψ_f trajectories are parallel with each other in the T_e-ψ_s plane under the $i_d = 0$ condition, as shown by the green lines in Fig. 9(a). The RMM manipulation procedure is similar to the DMM process, as illustrated in Fig. 9(b). The differences are the change direction of ψ_s and the shape of the MS lines.

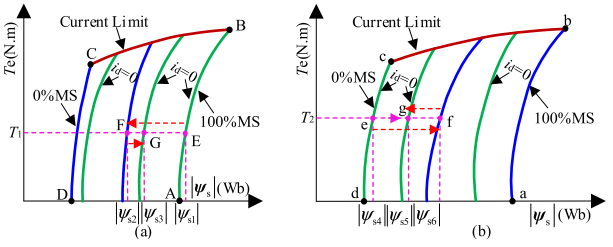

FIGURE 9. Torque-flux linkage ($T_e - \psi_s$) trajectories of the VFMM under different MSs. (a) DMM process. (b) RMM process.

The stator current is always constrained by the maximum winding current I_{smax}, which is presented as

$$\sqrt{i_d^2 + i_q^2} = |i_s| \leqslant I_{smax} \tag{13}$$

T_e and ψ_s can be acquired according to (8) and (9), respectively, by introducing i_d and i_q, which satisfy the condition of (13). Therefore, the T_e-ψ_s trajectory corresponding to the maximum current limiting condition can be obtained, as shown by the dark red line in Fig. 9.

C. SLIDING MODE CONTROL

Considering the variable parameters and large disturbances of VFMMs, an SMC is utilized to achieve robust dynamic behavior. By considering the fact that the conventional SMC suffers from large chattering, a super-twisting sliding mode (STSM) algorithm, which is a second-order scheme, is developed for the system. The sliding mode function $\boldsymbol{S} = [S_1\ S_2]^T$ is defined as

$$\begin{cases} S_1 = \psi_s^* - \psi_s \\ S_2 = T_e^* - T_e \end{cases} \tag{14}$$

The voltage equation in the rotor reference frame can be expressed as

$$\boldsymbol{u}_s = R_s \boldsymbol{i}_s + \frac{d\boldsymbol{\psi}_s}{dt} + j\omega_r \boldsymbol{\psi}_s \tag{15}$$

where $\boldsymbol{u}_s = u_d + \mathrm{j}u_q$, $\boldsymbol{i}_s = i_d + \mathrm{j}i_q$, and $\psi_s = \psi_d + \mathrm{j}\psi_q$ and represent the space vectors of the stator voltage, current and flux linkage, respectively. The derivatives of i_d, i_q and ω_r can be deduced as

$$\begin{cases} \dfrac{di_d}{dt} = -\dfrac{R_s}{L_d} i_d + \omega_r i_q + \dfrac{u_d}{L_d} \\ \dfrac{di_q}{dt} = -\dfrac{R_s}{L_q} i_q - \omega_r i_d + \dfrac{\psi_f}{L_q}\omega_r + \dfrac{u_q}{L_q} \\ \dfrac{d\omega_r}{dt} = \dfrac{3p\psi_f i_q}{2J} - \dfrac{T_L}{J} - \dfrac{B\omega_r}{J} \end{cases} \tag{16}$$

where T_L is the load torque, J is the inertia, and B is the viscosity coefficient. In the reference frame aligned with the stator flux vector, the derivative of the flux linkage is

$$\dot{\psi}_s = -R_s i_d + u_d \tag{17}$$

Therefore, the second derivative of S_2 can be deduced according to (16) and (17) as

$$\begin{aligned} \ddot{S}_1 &= -\ddot{\psi}_s = -\frac{R_s^2}{L_d} i_d + R_s \omega_r i_q + \frac{R_s}{L_d} u_d - \dot{u}_d \\ &= g(x,t) + f(x,t)\dot{u}_1 \end{aligned} \tag{18}$$

where u_1 is the input signal, which adopts u_d here. As R_s, L_d, i_d, i_q, ω_r, and u_d are all bounded parameters, the conditions of $0 \leq G_m \leq g(x,t) \leq G_M$ and $|f(x,t)| \leq F_M$ can be obtained, which are sufficient for u_1 to converge with the sliding surface. Here, G_m, G_M and F_M are the limit values of $g(x,t)$ and $f(x,t)$. Therefore, a finite-time convergence STSM stator flux linkage controller is obtained with a control constant $r = 0.5$ [35]:

$$\begin{cases} u_d = k_{pd}\sqrt{|S_1|}sign(S_1) + u_{d1} \\ \dot{u}_{d1} = k_{id} sign(S_1) \end{cases} \tag{19}$$

where k_{pd} and k_{id} meet the Lyapunov function stability conditions:

$$k_{id} > \frac{F_M}{G_M} > 0, \quad k_{pd} > \sqrt{\frac{2(k_{id}G_M + F_M)}{G_M}} \tag{20}$$

An STSM torque controller can also be achieved with a similar method. The derivatives of torque are deduced as

$$\begin{cases} \dot{T}_e = \dfrac{3}{2} p\psi_f \dfrac{di_q}{dt} \\ \ddot{S}_2 = -\ddot{T}_e = -\dfrac{3}{2} p\psi_f (-\dfrac{R_s}{L_q}\dfrac{di_q}{dt} - i_d\dfrac{d\omega_r}{dt} \\ \quad -\omega_r \dfrac{di_d}{dt} + \dfrac{\psi_f}{L_q}\dfrac{d\omega_r}{dt} + \dfrac{1}{L_q}\dot{u}_q) \\ = \dfrac{3}{2} p\psi_f [(\dfrac{R_s^2}{L_q^2} + \omega_r^2 - \dfrac{3p\psi_f^2}{2L_q J}) i_q \\ \quad -(\dfrac{R_s}{L_q}\omega_r + \dfrac{T_L}{J} + \dfrac{R_s}{L_d}\omega_r + \dfrac{B\omega_r}{J}) i_d \\ + \dfrac{3p\psi_f}{2J} i_d i_q + \dfrac{\psi_f}{L_q}(\dfrac{R_s}{L_q} + \dfrac{B}{J})\omega_r + \dfrac{R_s}{L_q^2} u_q \\ \quad + \dfrac{\omega_r}{L_d} u_d + \dfrac{\psi_f T_L}{L_q J} - \dfrac{1}{L_q}\dot{u}_q] \\ = s(x,t) + h(x,t)\dot{u}_2 \end{cases} \tag{21}$$

where u_2 is the input signal, which employs u_q here. The conditions of $0 \leq S_m \leq s(x,t) \leq S_M$ and $|h(x,t)| \leq H_M$ can be similarly obtained because R_s, L_d, L_q, i_d, i_q, ω_r, u_d, u_q, ψ_f, J and B are all bounded parameters, and the SM function is effective. Here, S_m, S_M and H_M are the limit values of $s(x,t)$ and $h(x,t)$. A finite-time convergence STSM torque controller can be obtained with a control constant $r = 0.5$ as well:

$$\begin{cases} u_q = k_{pq}\sqrt{|S_2|}sign(S_2) + u_{q1} \\ \dot{u}_{q1} = k_{iq} sign(S_2) \end{cases} \tag{22}$$

where k_{pq} and k_{iq} satisfy the Lyapunov function stability conditions:

$$k_{iq} > \frac{H_M}{S_M} > 0, \quad k_{pq} > \sqrt{\frac{2(k_{iq}S_M + H_M)}{S_M}} \tag{23}$$

According to (19) and (22), the proposed STSM direct torque and flux controllers are implemented in the stator reference frame, as shown by the block diagram in Fig. 10. The output signals of the STSM controllers are the reference voltages u_d and u_q. The space vector modulation is realized by u_α and u_β, which are acquired through the coordinate transformation of u_d and u_q, respectively.

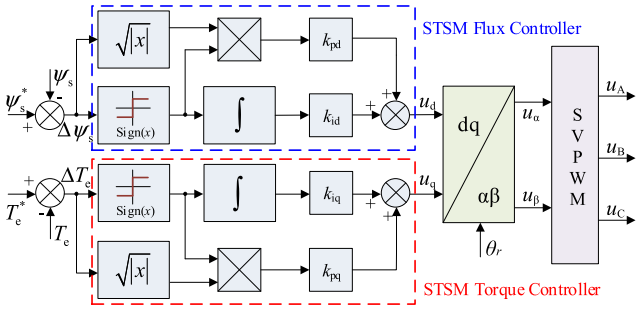

FIGURE 10. Block diagram of the STSM flux and torque controller.

IV. RESULTS AND DISCUSSIONS

The prototype and experimental system setup for this project are presented in Fig. 11. A magnetic powder brake acts as the torque load. A digital signal processor (DSP) TMS320F28335 and a complex programmable logic device (CPLD) EPM1270 are employed to build the central controller unit. The analog-to-digital sampling process is accomplished by an AD7329 chip with a sampling frequency of 10 kHz. The experimental data are acquired by a power analyzer with three current probes. The data transmission between the controller and the PC is realized by an RS-485 transceiver.

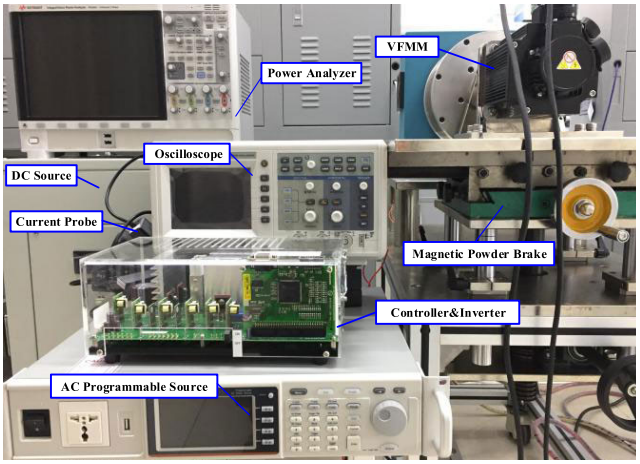

FIGURE 11. The prototype and experimental system.

A simulation model is built in MATLAB/Simulink to validate the behavior of the system. The rated parameters are tabulated in Table 1. The VFMM operates within a range from the rated speed to a higher speed, and the characteristics under different MSs are investigated.

TABLE 1. Rated Parameters of The VFMM

Description	Parameter (Unit)	Quantity
DC voltage	U_{DC} (V)	288
Rated speed	n_N (r/min)	1200
Rated power	P_N (W)	500
Rated load torque	T_N (Nm)	4
Stator resistance	R_s (Ω)	2
NdFeB PM flux (100% MS)	ψ_{f1} (Wb)	0.122
AlNiCo PM flux (100% MS)	ψ_{f2} (Wb)	0.019

A. RATED-STATE PERFORMANCE

The studied VFMM is driven by a power supply with the rated DC voltage. The load torque changes from load 1 (4 Nm) to load 2 (2 Nm) at 0.4 s. The static and dynamic torque performances of the machine with the conventional FOC method and the developed DTC method are compared in Fig. 12. Here, the DTC hysteresis bandwidth of the reference flux linkage and torque are taken as 0.02 Wb and 0.02 Nm, respectively.

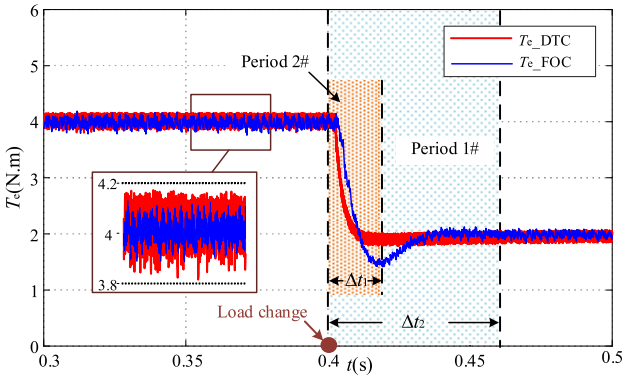

FIGURE 12. Torque waveforms of the DTC and FOC methods.

It can be seen from Fig. 12 that the torque curves of both the DTC (red line) and FOC (blue line) methods track the load torque well, verifying the validity of the control strategy. When the load is decreased from 4 Nm to 2 Nm at 0.4 s, both methods can achieve torque balance through the adjustment processes, which are represented by Period 1# and 2#. The process lasts Δt_1 in the FOC mode and Δt_2 in the DTC mode. It is noted that Δt_1 and Δt_2 are approximately 20 ms and 55 ms, respectively, indicating the rapid response capability of the DTC method during steady state. However, the DTC method produces a larger torque ripple compared with the FOC method, as shown in the partially enlarged detail of Fig. 12. The flux linkage trajectories of the DTC method under rated and light loads are quasi-circular and are achieved under the condition of id = 0 according to (10). Therefore, the trajectories of ψ_s, which vary with torque, never overlap under different loads.

To achieve a robust dynamic response and avoid large chattering at the same time, an STSM controller is creatively employed to control the VFMM. The speed waveforms of the machine with the DTC and STSM methods during the load change process are presented in Fig. 13. A rated voltage power supply is applied to drive the machine, and the load torque changes from 4 Nm to 2 Nm at 0.42 s. Here, the control gains of the STSM are $k_{pd} = k_{pq} = 100$ and $k_{id} = k_{iq} = 1000$. It can be seen from Fig. 13 that both methods can realize satisfactory speed tracking characteristics through the adjustment processes (Periods 3 and 4#). Period 3# lasts

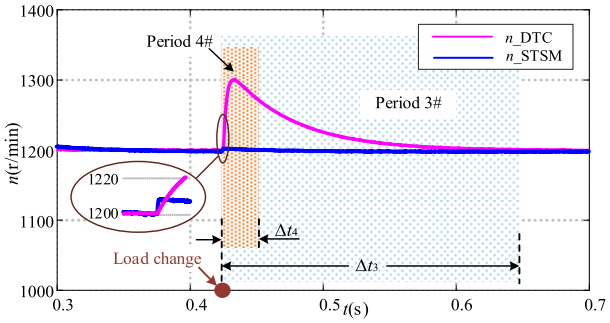

FIGURE 13. Speed waveforms of the DTC and STSM methods.

for Δt_3, while 4# lasts for Δt_4. Here, Δt_3 is approximately 220 ms, and Δt_4 is approximately 30 ms. It is noted that an overshoot (100 r/min) of 8.3% rated speed exists with the DTC method during the load change process. In contrast, the speed of the machine with the STSM method reaches the reference value in a finite time with scarcely any overshoot, which is only 10% of the DTC method. These results indicate that the proposed STSM scheme can reduce the speed fluctuation significantly during the process compared with the DTC method. In other words, the proposed algorithm has a strong robustness and small chattering even if load fluctuations exist.

B. MS MANIPULATION BEHAVIOR

The MS manipulation can be realized by applying a reference stator flux linkage pulse in a short period. Figs. 14∼16 show the flux linkage trajectory, the speed waveform and the d-axis current waveform during a DMM process. The amplitude of the flux linkage before the DMM is 0.186 Wb under a light load (2 Nm), as shown by trajectory 1# (blue line) in Fig. 14.

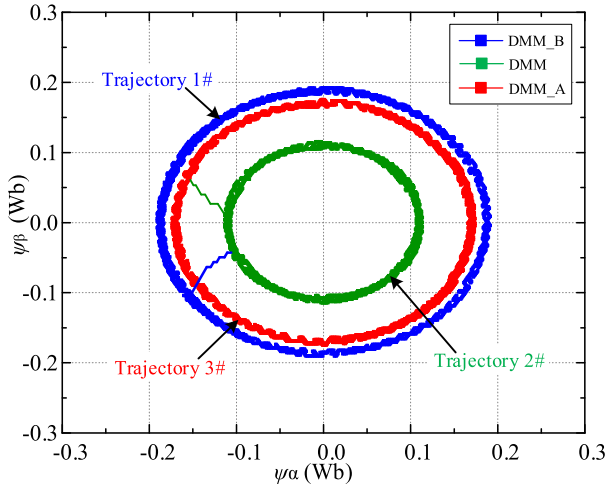

FIGURE 14. Flux linkage trajectories during the DMM process.

A reduced reference stator flux linkage pulse with an amplitude of 0.11 Wb is energized at 1 s and lasts for 50 ms, the trajectory of which in the $\psi_\beta - \psi_\alpha$ plane is denoted by trajectory 2# (green line). After the short period of the DMM, the stator flux linkage is reduced and retained approximately 0.166 Wb, as shown by trajectory 3# (red line). It can be seen from Fig. 15 that the actual speed waveform n_f1 (pink line) tracks the reference speed waveform n_g1 (blue dash line) with a small lag. The speed is 1200 r/min before the DMM process starting at 1 s and increases to 2000 r/min after the DMM period (Period 5#) and adjustment period (Period 6#). Δt_5 and Δt_6 represent the durations of Periods 5# and 6#, respectively, which approximately equal 50 ms and 120 ms, respectively. The speed curve shows a slight drop in the beginning of the DMM period and an overshoot of approximately 80 r/min during the adjustment period. It is noted that the speed range of the machine can be extended under a light load in a short period.

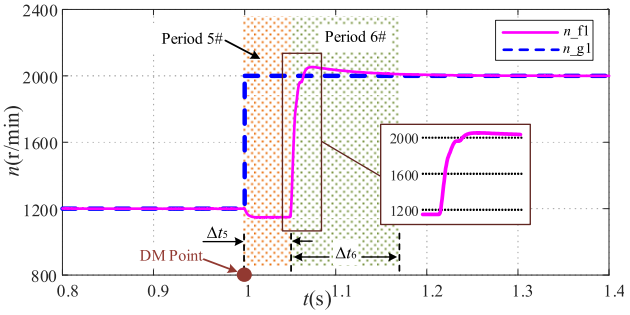

FIGURE 15. Speed waveforms during the DMM process.

Fig. 16 presents the d-axis current waveform during the DMM process. It is noted that a 7A DMM current is applied to alter the MS of the machine within 50 ms. The average value of the d-axis current is 0, and its fluctuation is approximately ± 0.3 A before and after the DMM process, indicating that the proposed ψ_s control scheme under the condition of $i_d = 0$ is validated.

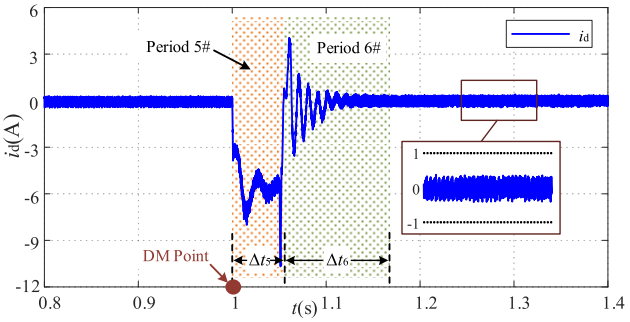

FIGURE 16. The d-axis current waveform during the DMM process.

The performance of the proposed method during an RMM process is also investigated and relevant waveforms are obtained. The flux linkage trajectories during the RMM process are shown in Fig. 17. It can be seen from Figs. 17 and 14 that the flux linkage is 0.166 Wb before the RMM under a light load (2 Nm) and is represented by trajectory 3# (red line). A new MS can be achieved by applying an increased reference stator flux linkage pulse in a short period. Here, the starting point of the RMM is at 2 s, and the pulse

lasts for 80 ms, with an amplitude of 0.5 Wb. Trajectory 4# (green line) reflects the flux linkage variation trend during the RMM process in the ψ_β-ψ_α plane. After the RMM process, the stator flux linkage is enhanced and restored to 0.186 Wb, as shown by trajectory 1# (blue line) in Figs. 17 and 14. Hence, a high-torque-output operation can be achieved under high-MS conditions. Trajectory 5# (pink line) is the flux linkage under the rated load (4 Nm) after the RMM process.

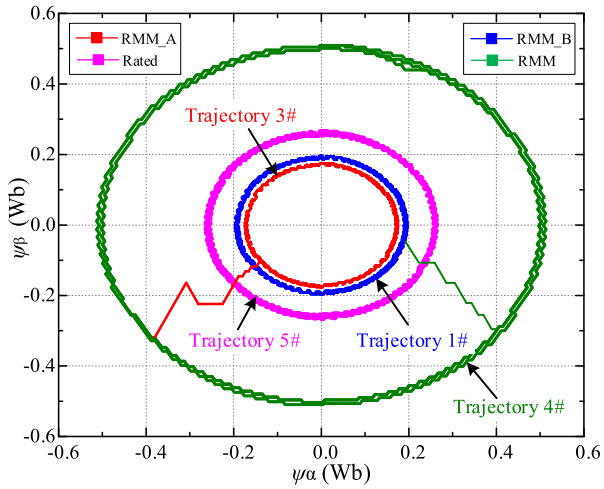

FIGURE 17. Flux linkage trajectories during the RMM process.

Actual speed n_f2 (red line) and reference speed n_g2 (blue dash line) waveforms during the RMM process are shown in Fig. 18. The machine operates in a high-speed region of 2000 r/min before the RMM starting at 2 s. Speed n_f2 tracks n_g2 very well through the RMM period (Period 7#) and adjustment period (Period 8#). Period 7# lasts for $\Delta t_7 (\approx$ 80 ms) while 8# for $\Delta t_8 (\approx$ 180 ms). A speed fluctuation and an overshoot can be observed because of the current variation and load increasement during the RMM process.

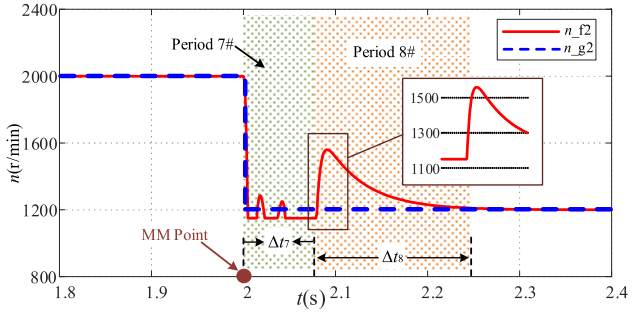

FIGURE 18. The speed waveforms during the RMM process.

Fig. 19 exhibits the d-axis current waveform during the RMM process. The RMM procedure consists of an RMM period (Period 7#) and an adjustment period (Period 8#), which is similar to the DMM process. It can be seen that the steady average value of the d-axis current is 0, with a fluctuation of $\pm$ 0.3 A, which contributes to the proposed ψ_s

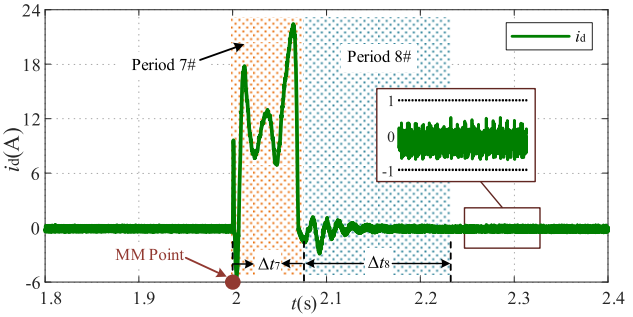

FIGURE 19. The d-axis current waveform during the RMM process.

control scheme. For the sake of full magnetization, the amplitude of the magnetizing current ($\approx$ 22 A) is larger, and the manipulation period ($\approx$ 80 ms) is longer during the RMM process compared with those of the DMM process.

The flux trajectories (ψ_f - ψ_s) during the DMM (blue line) and RMM (red line) processes are compared in Fig. 20. The PM flux linkage ψ_f under a light load is used to estimate the MS. It can be seen from Fig. 20 that the MS of the machine varies with a reference stator flux linkage ψ_s pulse. The PM magnetization level is a function of the amplitude of the ψ_s pulse, where the full RMM and DMM refer to 0.626 Wb and 0.0968 Wb, respectively.

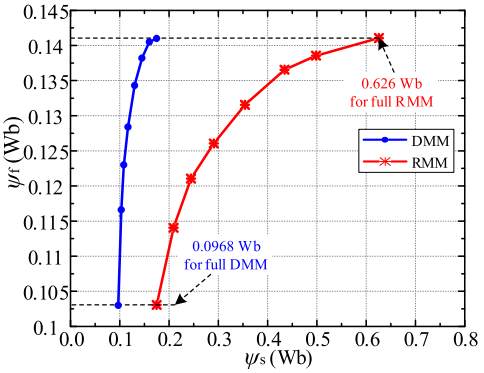

FIGURE 20. The flux trajectories ($\psi_f - \psi_s$) during MS manipulations.

The torque-speed curves of the investigated VFMM with and without FW are shown in Fig. 21. The curve (blue line) labeled with "without FW" refers to the T_e-n performance of the machine with the conventional DTC method, while the other curve (red line) represents that with the proposed FW method. In the constant torque region, the torques can approximately maintain 4 Nm for both control schemes, as shown by line AB. When n exceeds n_B (1200 r/min), the machine operates in CPSR, for which the torque is inversely proportional to the rotational speed. With the conventional DTC method, the T_e-n curve is CPSR 1#, and the maximum speed under no-load condition is n_D (4000 r/min). A DMM is conducted in point C where the speed reaches n_C (1400 r/min). Consequently, a new torque-speed curve is obtained, as shown by curve BCE. It can be observed that the maximum speed under the no-load condition is beyond n_E (5000 r/min). This result shows that the CPSR of the machine is extended to the combination of CPSR 1# and 2# by applying the proposed FW

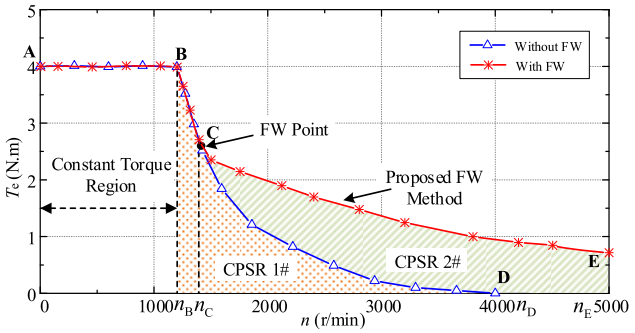

FIGURE 21. The torque-speed curves ($T_e - n$) with or without the FW method.

control scheme. The results and analyses abovementioned indicate that the proposed method can effectively improve the FW capability and extend the CPSR compared with the conventional DTC method.

Fig. 22 shows the current changes of phase A during the DMM and RMM processes. The machine operates under a light load (2 Nm) during the processes to simulate the high-speed cruising operation of an EV. The phase current achieves a steady state at Steady point 1# after demagnetization, and its peak-to-peak (P-P) value increases from 6.4 A to 7.4 A, which represents an increase of 15.6%. In contrast, the P-P value of the phase current decreases from 7.4 A to 6.4 A after re-magnetization. The current increases during both processes, while the amplitude is larger and the duration is longer for the RMM process to achieve a full re-magnetization. It is noted that the speed increases after the DMM process and is restored to the rated value through the RMM process.

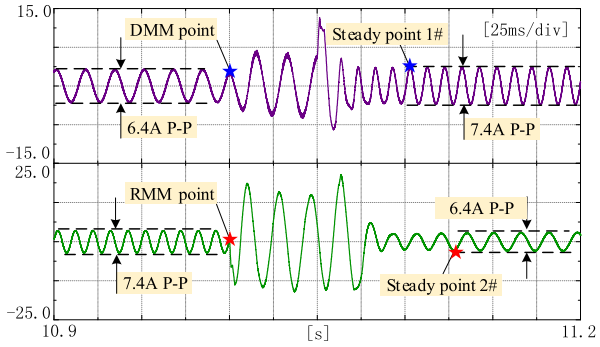

FIGURE 22. Current changes of phase A during the DMM and RMM processes.

The torque-flux (T_e-ψ_s) trajectory over time during the DMM process is obtained, as shown by the three-dimensional blue curve in Fig. 23. The curve's projection (red line) onto the T_e-ψ_s plane is also presented. The working point moves from the DMM point to Steady point 1#, and the stator flux linkage varies for the duration of the process. In this period, the flux linkage operating point moves from P to M and then stabilizes at Q, validating the effectiveness of the proposed demagnetization method. It can be seen that some torque ripples exist during the process. However, they have

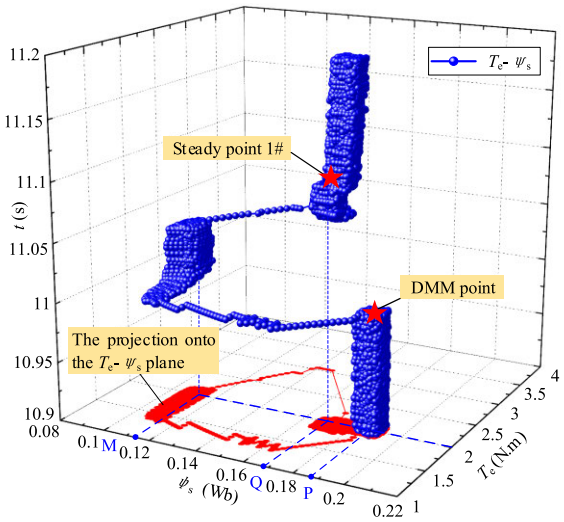

FIGURE 23. Torque-flux linkage ($T_e - \psi_s$) trajectory during the DMM process.

less influence within a short period (100 ms), and the torque remains constant during the entire procedure.

The proposed VFMM control system can perform effective flux linkage adjustment while involving negligible MS manipulation loss and eliminating complicated current control. Nevertheless, more sufficient experimentation and further research are needed. Future work should focus on the efficiency tests, transient behavior of the MS controller, and the control characteristics of diverse intelligent algorithms.

V. CONCLUSION

This paper proposes a second-order SM-based DTC strategy for a hybrid PM VFMM without sophisticated current control efforts. The scheme combines the advantages of conventional DTC with the variable-flux characteristics of VFMMs. The method of the DTC incorporating the $i_d = 0$ condition is utilized under normal operations, and reference flux-weakening or flux-strengthening pulses are energized in MS manipulation regions. By adopting this method, the dynamic response is improved and the flux adjustment is simplified, effectively extending the CPSR of the machine. The proposed super-twisting SM controller reduces the speed fluctuation to 10% of the conventional DTC scheme during the load change processes and exhibits independence from the machine's inductance. The results demonstrate that the studied VFMM can achieve a wide speed, high efficiency, and strong robustness performance when the SM-based DTC and MS control are taken synthetically. Overall, the proposed VFMM system is a promising choice for wide-CPSR requirement applications, e.g., electric vehicles.

REFERENCES

[1] Z. Q. Zhu, *Permanent Magnet Machines for Traction Applications*. Hoboken, NJ, USA: Wiley, 2014, pp. 1–2.
[2] T. M. Jahns, "Motion control with permanent-magnet AC machines," *Proc. IEEE*, vol. 82, no. 8, pp. 1241–1252, Aug. 1994.
[3] C. C. Chan, K. T. Chau, J. Z. Jiang, W. Xia, M. Zhu, and R. Zhang, "Novel permanent magnet motor drives for electric vehicles," *IEEE Trans. Ind. Electron.*, vol. 43, no. 2, pp. 331–339, Apr. 1996.

[4] K. T. Chau, C. C. Chan, and C. Liu, "Overview of permanent-magnet brushless drives for electric and hybrid electric vehicles," *IEEE Trans. Ind. Electron.*, vol. 55, no. 6, pp. 2246–2257, Jun. 2008.
[5] M. Ehsani, K. M. Rahman, and H. A. Toliyat, "Propulsion system design of electric and hybrid vehicles," *IEEE Trans. Ind. Electron.*, vol. 44, no. 1, pp. 19–27, Feb. 1997.
[6] S. Morimoto, M. Sanada, and Y. Takeda, "Wide-speed operation of interior permanent magnet synchronous motors with high-performance current regulator," *IEEE Trans. Ind. Appl.*, vol. 30, no. 4, pp. 920–926, Jul. 1994.
[7] V. Ostovic, "Memory motors," *IEEE Ind. Appl. Mag.*, vol. 9, no. 1, pp. 52–61, Jan. 2003.
[8] K. Sakai, K. Yuki, Y. Hashiba, N. Takahashi, and K. Yasui, "Principle of the variable-magnetic-force memory motor," in *Proc. Int. Conf. Electr. Mach. Syst.*, Nov. 2009, pp. 1–6.
[9] H. Yang, S. Lyu, H. Lin, Z. Q. Zhu, F. Peng, E. Zhuang, S. Fang, and Y. Huang, "Stepwise magnetization control strategy for DC-magnetized memory machine," *IEEE Trans. Ind. Electron.*, vol. 66, no. 6, pp. 4273–4285, Jun. 2019.
[10] S. Lyu, H. Yang, H. Lin, Z. Q. Zhu, H. Zheng, and Z. Pan, "Influence of design parameters on on-load demagnetization characteristics of switched flux hybrid magnet memory machine," *IEEE Trans. Magn.*, vol. 55, no. 7, pp. 1–5, Jul. 2019.
[11] S. Maekawa, K. Yuki, M. Matsushita, I. Nitta, Y. Hasegawa, T. Shiga, T. Hosoito, K. Nagai, and H. Kubota, "Study of the magnetization method suitable for fractional-slot concentrated-winding variable magnetomotive-force memory motor," *IEEE Trans. Power Electron.*, vol. 29, no. 9, pp. 4877–4887, Sep. 2014.
[12] C.-Y. Yu, T. Fukushige, N. Limsuwan, T. Kato, D. D. Reigosa, and R. D. Lorenz, "Variable-flux machine torque estimation and pulsating torque mitigation during magnetization state manipulation," *IEEE Trans. Ind. Appl.*, vol. 50, no. 5, pp. 3414–3422, Sep. 2014.
[13] T. Fukushige, N. Limsuwan, T. Kato, K. Akatsu, and R. D. Lorenz, "Efficiency contours and loss minimization over a driving cycle of a variable flux-intensifying machine," *IEEE Trans. Ind. Appl.*, vol. 51, no. 4, pp. 2984–2989, Jul. 2015.
[14] B. S. Gagas, K. Sasaki, T. Fukushige, A. Athavale, T. Kato, and R. D. Lorenz, "Analysis of magnetizing trajectories for variable flux pm synchronous machines considering voltage, high-speed capability, torque ripple, and time duration," *IEEE Trans. Ind. Appl.*, vol. 52, no. 5, pp. 4029–4038, Sep. 2016.
[15] A. Athavale, D. J. Erato, and R. D. Lorenz, "Enabling driving cycle loss reduction in variable flux PMSMs via closed-loop magnetization state control," *IEEE Trans. Ind. Appl.*, vol. 54, no. 4, pp. 3350–3359, Jul. 2018.
[16] B. S. Gagas, K. Sasaki, A. Athavale, T. Kato, and R. D. Lorenz, "Magnet temperature effects on the useful properties of variable flux PM synchronous machines and a mitigating method for magnetization changes," *IEEE Trans. Ind. Appl.*, vol. 53, no. 3, pp. 2189–2199, May 2017.
[17] R. Thike and P. Pillay, "Characterization of a variable flux machine for transportation using a vector-controlled drive," *IEEE Trans. Transp. Electrific.*, vol. 4, no. 2, pp. 494–505, Jun. 2018.
[18] A. M. Aljehaimi and P. Pillay, "Novel flux linkage estimation algorithm for a variable flux PMSM," *IEEE Trans. Ind. Appl.*, vol. 54, no. 3, pp. 2319–2335, May 2018.
[19] J. Chen, J. Li, and R. Qu, "Maximum-torque-per-ampere and magnetization-state control of a variable-flux permanent magnet machine," *IEEE Trans. Ind. Electron.*, vol. 65, no. 2, pp. 1158–1169, Feb. 2018.
[20] C. Yu and K. T. Chau, "Design, analysis, and control of dc-excited memory motors," *IEEE Trans. Energy Convers.*, vol. 26, no. 2, pp. 479–489, Jun. 2011.
[21] C. Yu and K. T. Chau, "Dual-mode operation of DC-excited memory motors under flux regulation," *IEEE Trans. Ind. Appl.*, vol. 47, no. 5, pp. 2031–2041, Sep. 2011.
[22] F. Li, K. T. Chau, and C. Liu, "Pole-changing flux-weakening DC-excited dual-memory machines for electric vehicles," *IEEE Trans. Energy Convers.*, vol. 31, no. 1, pp. 27–36, Mar. 2016.
[23] X. Zhu, Z. Xiang, L. Quan, W. Wu, and Y. Du, "Multimode optimization design methodology for a flux-controllable stator permanent magnet memory motor considering driving cycles," *IEEE Trans. Ind. Electron.*, vol. 65, no. 7, pp. 5353–5366, Jul. 2018.
[24] G. Yang, M. Lin, N. Li, G. Tan, and B. Zhang, "Flux-weakening control combined with magnetization state manipulation of hybrid permanent magnet axial field flux-switching memory machine," *IEEE Trans. Energy Convers.*, vol. 33, no. 4, pp. 2210–2219, Dec. 2018.
[25] I. Takahashi and T. Noguchi, "A new quick-response and high-efficiency control strategy of an induction motor," *IEEE Trans. Ind. Appl.*, vol. IA-22, no. 5, pp. 820–827, Sep. 1986.
[26] L. Zhong, M. F. Rahman, W. Y. Hu, and K. W. Lim, "Analysis of direct torque control in permanent magnet synchronous motor drives," *IEEE Trans. Power Electron.*, vol. 12, no. 3, pp. 528–536, May 1997.
[27] T. Inoue, Y. Inoue, S. Morimoto, and M. Sanada, "Maximum torque per ampere control of a direct torque-controlled PMSM in a stator flux linkage synchronous frame," *IEEE Trans. Ind. Appl.*, vol. 52, no. 3, pp. 2360–2367, May 2016.
[28] A. Shinohara, Y. Inoue, S. Morimoto, and M. Sanada, "Maximum torque per ampere control in stator flux linkage synchronous frame for DTC-based PMSM drives without using q-axis inductance," *IEEE Trans. Ind. Appl.*, vol. 53, no. 4, pp. 3663–3671, Jul. 2017.
[29] M. F. Rahman, L. Zhong, and K. W. Lim, "A direct torque-controlled interior permanent magnet synchronous motor drive incorporating field weakening," *IEEE Trans. Ind. Appl.*, vol. 34, no. 6, pp. 1246–1253, Nov. 1998.
[30] Y. Inoue, S. Morimoto, and M. Sanada, "Comparative study of PMSM drive systems based on current control and direct torque control in flux-weakening control region," *IEEE Trans. Ind. Appl.*, vol. 48, no. 6, pp. 2382–2389, Nov. 2012.
[31] Z. Xu and M. F. Rahman, "Direct torque and flux regulation of an IPM synchronous motor drive using variable structure control approach," *IEEE Trans. Power Electron.*, vol. 22, no. 6, pp. 2487–2498, Nov. 2007.
[32] G. Foo and M. F. Rahman, "Sensorless sliding-mode MTPA control of an IPM synchronous motor drive using a sliding-mode observer and HF signal injection," *IEEE Trans. Ind. Electron.*, vol. 57, no. 4, pp. 1270–1278, Apr. 2010.
[33] G. H. B. Foo and M. F. Rahman, "Direct torque control of an IPM-synchronous motor drive at very low speed using a sliding-mode stator flux observer," *IEEE Trans. Power Electron.*, vol. 25, no. 4, pp. 933–942, Apr. 2010.
[34] J. J. Slotine, W. Li, and P. Hall, *Applied Nonlinear Control: United States Edition*. London, U.K.: Pearson, 1990.
[35] A. Levant, "Principles of 2-sliding mode design," *Automatica*, vol. 43, no. 4, pp. 576–586, Apr. 2007.

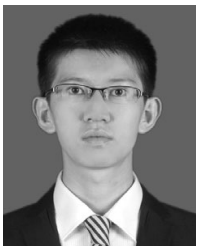

WEI WANG (Student Member, IEEE) was born in Inner Mongolia, China, in 1989. He received the B.S. and M.S. degrees in electrical engineering from Automation Faculty, Northwestern Polytechnical University, Xi'an, China, in 2011 and 2014, respectively. He is currently pursuing the Ph.D. degree in electrical engineering with Southeast University, Nanjing, China. Since 2014, he has been with the Ordos Institute of Technology, where he is a Lecturer with the School of Information Engineering. His research interests include control of novel permanent magnet machines and power electronics.

HEYUN LIN (Senior Member, IEEE) received the B.S., M.S., and Ph.D. degrees in electrical engineering from the Nanjing University of Aeronautics and Astronautics, Nanjing, China, in 1985, 1989, and 1992, respectively.

From 1992 to 1994, he was a Postdoctoral Fellow with Southeast University, Nanjing. In 1994, he joined the School of Electrical Engineering, Southeast University, as an Associate Professor and became a Full Professor, since 2000. He is the author of more than 200 technical articles and the holder of 60 patents. His main research is related to the design, analysis and control of permanent magnet motor, intelligent electrical apparatus and electromagnetic field numerical analysis. He is a Fellow of the IET, a member of the Electrical Motor and Apparatus Committee of Jiangsu Province, and a Senior Member of the China Society of Electrical Engineering and China Electrotechnical Society.

HUI YANG (Member, IEEE) was born in Changning, Hunan, China. He received the B.Eng. degree from the Dalian University of Technology, Dalian, China, in 2011, and the Ph.D. degree from Southeast University, Nanjing, China, in 2016, both in electrical engineering.

From 2014 to 2015, he was supported by the China Scholarship Council through a one-year joint the Ph.D. studentship with the University of Sheffield, Sheffield, U.K. Since 2016, he has been with Southeast University, where he is an Associate Professor with the School of Electrical Engineering. Since 2019, he has served as a Postdoctoral Research Fellow with the School of Electrical Engineering, The Hong Kong Polytechnic University. His research interest includes design and analysis of novel permanent-magnet machines with particular reference to variable-flux machines for electric vehicles and renewable energy applications. He was a recipient of the Best Paper Awards in ICEMS 2014 and EVER 2015, and the holder of 11 patents.

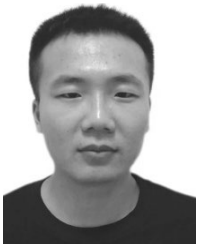

WEI LIU (Student Member, IEEE) was born in Shandong, China, in 1992. He received the B.Eng. degree from the Shandong University of Technology, China, in 2015, and the M.Sc. degree from the North University of China, China, in 2018. He is currently pursuing the Ph.D. degree with the Southeast University, Nanjing, China. His current research interest includes the design, analysis, and optimization of electrical machine especially variable flux memory machine.

SHUKANG LYU received the B.Eng. degree in new energy science and engineering from Hohai University, Nanjing, China, in 2016. He is currently pursuing the Ph.D. degree in electrical engineering with Southeast University, Nanjing. His research interest includes control strategies for permanent magnet machines and power electronics.